



# Graphene nanoplatelets reinforced Al-Cu-Mg composite fabricated using laser powder bed fusion: microstructure, mechanical properties, and wear behaviour

Mulla Ahmet Pekok<sup>1,2</sup> · Rossitza Setchi<sup>2</sup> · Michael Ryan<sup>2</sup> · Emmanuel Brousseau<sup>2</sup> · Quanquan Han<sup>3</sup> · Dongdong Gu<sup>4</sup>

Received: 30 March 2023 / Accepted: 20 July 2023  
© The Author(s) 2023

## Abstract

Aluminium-based metal matrix composites reinforced with graphene (Gr) and its derivatives have been reported as promising composites due to their superior properties such as strength, damage tolerance, fatigue resistance, and density. However, the crack and porosity susceptibility of Aluminium 2024 Alloy (AA2024) with added Gr when fabricated using additive manufacturing techniques is not sufficiently well understood. The present work addresses this knowledge gap by focusing on the effect of graphene nanoplatelets (GNPs) and scanning speed on the AA2024 composites' wear performance and microstructural and mechanical properties of specimens fabricated using laser powder bed fusion (LPBF). The experimental findings demonstrate that up to 0.5% presence of Gr in the composite improves its crystallite size and microhardness by up to 37.6% and 45%, respectively; however, it increases the porosity and crack formation due to the high laser power requirement. Moreover, the composites' macroscale scratch and nanoscale wear performances showed improvements by up to 50% and 56% with higher Gr concentration (0.5%), suggesting that Gr is distributed uniformly in the structure. The improved understanding of the relationship between microstructure and mechanical characteristics of the GNPs/Al2024 composites fabricated using LPBF in terms of cracking and porosity formation is another significant contribution of this work.

**Keywords** Laser powder bed fusion · Aluminium 2024 Alloy · Graphene nanoplatelets · Mechanical properties · Microstructure · Wear behaviour

## 1 Introduction

The unique properties of graphene (Gr) and its derivatives have attracted the attention of researchers worldwide. The reason behind this interest is predominantly their excellent electrical (6000 S/cm) and thermal (5300 W/make)

conductivity, high specific surface area (2630 m<sup>2</sup>/g), unique two-dimensional honeycomb lattice structure, and low density (1.8 g/cm<sup>3</sup>) [1] as well as their high tensile strength (130 GPa) and elastic modulus (0.5–1 TPa) [2]. Due to these properties, Gr-based nanomaterials are frequently used as reinforcement elements in new applications in material science, to improve the mechanical properties of known metals such as aluminium and its alloys.

High-strength Al-Cu-Mg alloys are adopted in many engineering industries such as aerospace, automotive, defence, marine, construction, and medicine because of their good resistance to corrosion, electrical and thermal conductivity, and density [3]. However, some of the aluminium alloys, including Aluminium 2024 Alloy (AA2024), demonstrate significant drawbacks such as high reflectivity (93% of the laser energy at 1- $\mu$ m wavelength [4]), high sensitivity to relative cracking as a result of superior residual thermal stress [5], and poor flowability owing to the non-spherical morphology of the powder, which is very important for

✉ Rossitza Setchi  
Setchi@cardiff.ac.uk

<sup>1</sup> Engineering Faculty, Mechanical Engineering, Osmaniye Korkut Ata University, 80000 Osmaniye, Turkey

<sup>2</sup> Cardiff School of Engineering, Cardiff University, Cardiff CF24 3AA, UK

<sup>3</sup> School of Mechanical Engineering, Shandong University, Jinan 250061, China

<sup>4</sup> College of Materials Science and Technology, Nanjing University of Aeronautics and Astronautics, Nanjing 210016, China

additive manufacturing applications and primarily affect the mechanical properties of the as-fabricated samples. Carbon-based allotropes have been successfully used as reinforcement elements in some studies [6, 7] to improve the alloys' mechanical properties using different fabrication techniques.

The reinforcement of Gr and its derivatives, however, has some unique challenges. One of the biggest problems for Gr as a reinforcement is agglomeration due to the van der Waals forces and  $\pi$ – $\pi$  interactions [8]. The ball milling technique is often used to achieve uniform dispersion of Gr in composites as it provides sufficient output energy to break strong van der Waals interlayer bonds of Gr and offers a large variety of processing parameters such as milling and pause time, rotation speed, process control agent (PCA), and ball-to-powder weight ratio [9]. However, the changes in the particle morphology during the ball milling process have to be considered carefully.

Studies have shown that continuously applied impact energy by the milling balls provides more uniform dispersion of reinforcement material but changes the powder morphology from near-spherical to near-flat shape [9]. Another drawback of the Gr is its reactivity with aluminium. It has been reported that Gr reacts with Al over 500 °C and forms a brittle  $\text{Al}_4\text{C}_3$  phase [10]. A certain amount of  $\text{Al}_4\text{C}_3$  can improve wettability and mechanical properties [11], but the  $\text{Al}_4\text{C}_3$  structures formed at the interface between the metal matrix (AA2024) and carbonaceous materials (GNPs) adversely affect the mechanical properties of the composite [12], which is another limitation highlighted in the literature [13].

Nowadays, additive manufacturing technologies meet the requirements of many high-value manufacturing sectors due to benefits such as rapid and easy fabrication of complex geometries, flexibility in design, minimisation of waste, and near-net-shape production [14]. In particular, laser-based additive manufacturing such as laser powder bed fusion (LPBF) offer significant potential and an unique opportunity for a wide range of metals and their alloys, such as stainless steel, nickel, aluminium, titanium, magnesium, copper, and many others [15].

Gr/AA2024 composites have been studied using fabrication techniques such as hot-extrusion pressure, hot rolling, and powder metallurgy. However, the effect of Gr on AA2024 when fabricated using LPBF is not well understood. Accordingly, this study addresses the knowledge gap in this area by investigating the wear performance and microstructural and mechanical properties of graphene nanoplatelet (GNP)-reinforced AA2024 composites, fabricated using LPBF. The focus of this work is on the effect of various scanning speeds (195 to 727 mm/s) and weight Gr ratios (0.1 to 0.5 wt.%) on the microstructure, microhardness, density, wear performance, and tensile properties of the composites. Hence, the main contribution of this research

is developing an in-depth understanding of the relationship between the Gr concentration, LPBF processing parameters, and the mechanical properties of the fabricated composites. An additional contribution is the comparison between the macroscale and nanoscale wear performance of the composites. Finally, this work offers some practical recommendations in terms of process parameters and concentration of the reinforced element.

## 2 Experimental procedure

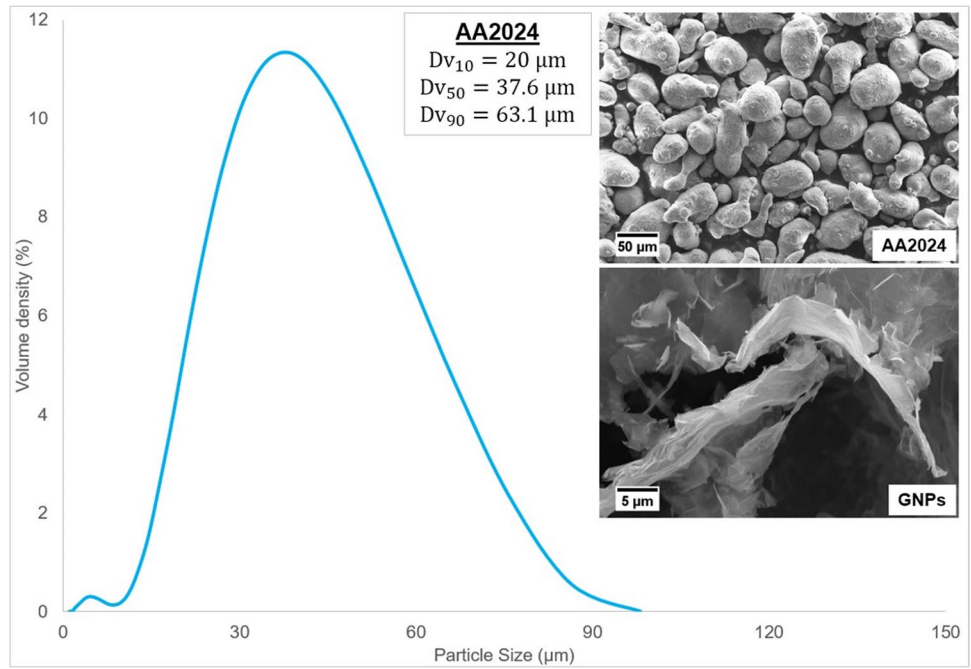
### 2.1 Materials and processing

This study used gas atomised AA2024 powder, which is obtained from Carpenter Additive Technology Corporation (Philadelphia, USA). The chemical composition of the alloy was 4.9Cu-1.8Mg-0.9Mn-0.5Si-0.5Fe-bal. Al (wt.%). The alloy particle size differentiated between 2 and 86  $\mu\text{m}$ , while the average particle size was 37  $\mu\text{m}$ , which was determined by a Malvern Mastersizer-3000 (Malvern, UK) particle size characterisation machine (Fig. 1). The alloy had a 2.7 g/cm<sup>3</sup> relative density and melting point of 660 °C. On the other hand, GNPs, which were attained from Sigma-Aldrich Company Ltd. (Dorset, UK), had a 50–80 m<sup>2</sup>/g surface area and a 3652 °C melting point.

A laboratory-size planetary ball milling machine (PULVERISETTE 5 classic line, Fritsch GmbH, Idar-Oberstein, Germany) was used to mill the GNPs/AA2024 composite under different weight ratios of Gr (0.1, 0.2, and 0.5 wt.%). Each milling bowl contains 800 g of milling balls and 80 g of powder (the ball-to-powder weight ratio is 10:1). For the 0.1 wt% Gr-reinforced composite, the powder consists of 78.32 g of AA2024, 1.6 g of stearic acid ( $\text{C}_{18}\text{H}_{36}\text{O}_2$ ), and 0.08 g of GNPs. Gr concentration was adjusted to 0.16 g and 0.4 g for 0.2 and 0.5 wt.% Gr-reinforced composites, respectively. The previous publication of the authors provides further detail on the milling procedure [16]. The advanced composite powders have been produced using low-energy ball milling (LEBM). The milling speed (100 rpm), milling time (4 h), and percentage of stearic acid (2%) as a PCA were kept constant during the LEBM process. The optimisation of the ball milling speed [17] and wide range of milling time [16] were reported in previous studies of the authors, which concluded that while high-energy ball milling immediately causes a substantial change in the powder morphology, LEBM at longer milling times provides a uniform distribution of Gr. Further details have been given in [16, 17].

An LPBF machine (Renishaw AM250 system, Gloucestershire, UK) was used to fabricate cubic and tensile testing specimens for different percentages of the composites. Reduced build volume with plate dimensions of 78 × 78 mm<sup>2</sup>

**Fig. 1** The particle size distribution and SEM images of the as-received AA2024 alloy and GNPs



was engaged to the machine to save power and time. The fabrication process from the powder preparation to specimens is illustrated in Fig. 2. Laser scanning speed varied between 195, 380, 500, and 727 mm/s. Laser power (200 W), layer thickness (25 μm), and hatch spacing (80 μm) were kept constant during the build. The optimisation of laser power, point distance, and

scanning speed was reported in a previous study of the authors [18]. The scanning speed ( $V$ ) was calculated using laser exposure time as outlined in the previous work of the authors [18]:

$$V = d_p / (T_e + T_d) \tag{1}$$

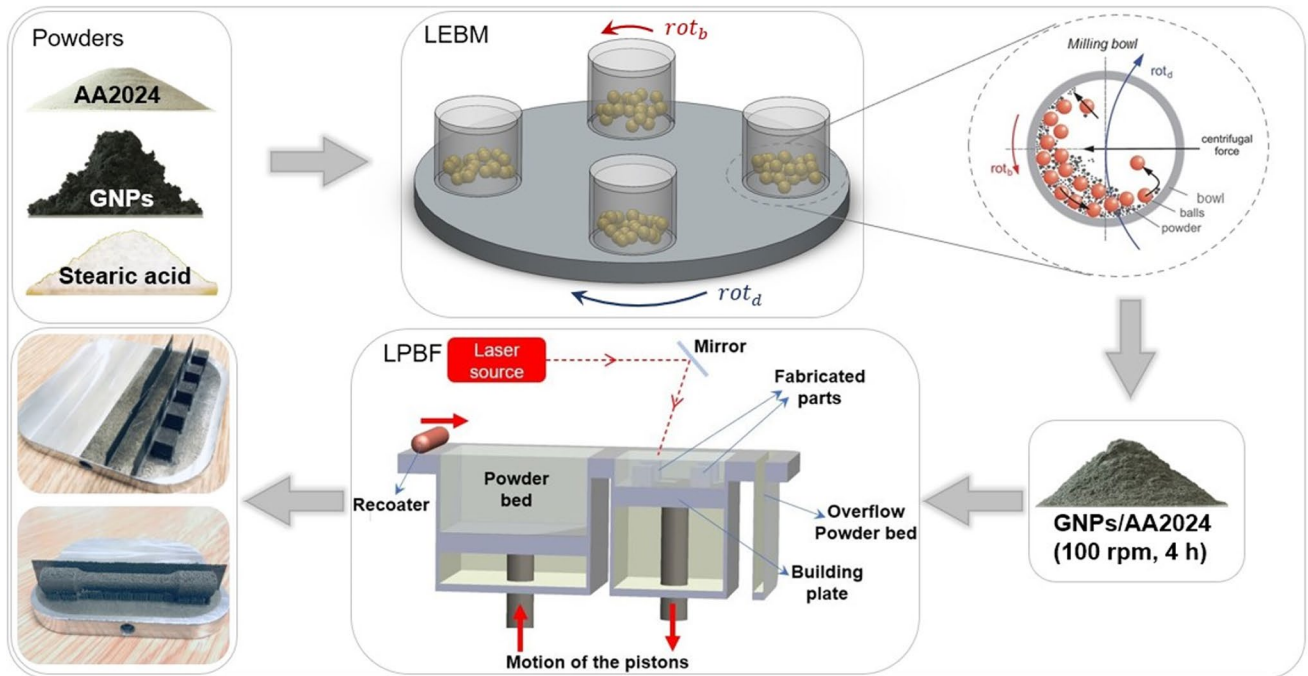


**Fig. 2** Schematic diagram of the fabrication steps from powder preparation to building LPBF samples

where  $d_p$  (80  $\mu\text{m}$ ) is the point distance between laser spots,  $T_e$  (400, 200, 150, 100  $\mu\text{s}$ ) is the laser exposure time at one point, and  $T_d$  (10  $\mu\text{s}$ ), which is a constant value for the AM machine, is the laser delay time from one point to another.

The ASTM-E8 tensile testing standard with the layers perpendicular to the loading direction was used to produce tensile test specimens. The barriers next to the cubic and tensile specimens were designed to keep an adequate amount of powder in the operation region and reduce the negative effect of short feeding during the fabrication.

## 2.2 Characterisation

The specimens were fabricated on 2 mm supports, and the chamber was filled with argon gas in order to prevent the as-fabricated sample from oxidation during the building process. Archimedes' density (also known as bulk density) of the samples was determined using a density determination kit.

Next, the fabricated cubic samples were mounted in an electrically conductive resin so that the building direction was parallel to the analysed surface. The surfaces were sanded with 200, 400, 800, 1200, 2400, and 4000 grid silicon carbide sandpapers first and then polished with 5, 3, and 0.1  $\mu\text{m}$  polishing cloths using diamond suspensions and aluminium oxide lubricant in order to obtain a smooth surface for observation. Next, a Nikon eclipse LV-100 (NY, USA) Optical Microscope (OM) was used to examine the surface, and ImageJ software was employed to calculate the relative density of the specimens from the obtained OM images. Three different layers of the specimens were examined in order to obtain more accurate results. In addition, Keller's reagent (5 ml  $\text{HNO}_3$ , 3 ml  $\text{HCl}$ , 2 ml  $\text{HF}$ , and 190 ml distilled water) was applied on the surface for about 30 to 40 s to observe the microstructure of the specimens.

Phase identification of the powders and the samples was performed using a Siemens/Bruker D5000 X-ray powder diffraction machine with  $\text{CuK}\alpha$  radiation ( $\lambda = 0.15406 \text{ nm}$ ) at 40 kV and 30 mA settings. The average crystallite size ( $D$ ) of the milled powder and fabricated composites was calculated as follows:

$$D = (K * \lambda) / (\beta * \cos \theta) \quad (2)$$

where  $K$  is a Scherrer constant close to unity (0.9),  $\lambda$  is the wavelength of the  $\text{CuK}\alpha$  X-ray radiation (0.15406 nm),  $\beta$  is the line broadening at full width at half maximum, and  $\theta$  is the Bragg's angle.

A Nova 330/360 IMP Innovatest (Maastricht, Netherlands) microhardness test machine was used to measure the Vickers microhardness performance of the samples under 200 g load, 10 s dwell time.

Afterwards, uniaxial tensile tests were performed at room temperature using a Zwick/Roell tensile tester with a strain rate of 0.001 mm/s. Rotating pin-on-disc wear tests were conducted under 1 kg normal load, 25 rpm rotation speed, 30 min sliding time, and 5 mm rotation diameter at room temperature and quiet place in order to eliminate the negative effect of temperature and vibration. Diameter grade 100 hardened AISI-52100 chrome-steel balls (3/8") were placed on the test pin. The friction signals ( $F$ ), recorded for each sample during the tests, were used to calculate the friction coefficients ( $\mu$ ), as recommended by the ASTM D3702-94 standard:

$$\mu = F * A / N \quad (3)$$

where  $A$  denotes the mechanical advantage of the lever arm (approximately 0.6 for the present experiment), and  $N$  represents the normal load. Additionally, the wear rate ( $\omega_r$ ) of the specimens after the wear test was calculated as [19]

$$\omega_r = V_{\Delta} / N * L \quad (4)$$

where  $V_{\Delta}$  and  $L$  represent the volume of loss and sliding distance, respectively. The volume of loss was determined by dividing the weight loss ( $W_{\Delta}$ ) by the density of the specimens as recommended by the ASTM G99-95a standard. The wear test was repeated three times for each specimen to verify the results.

Atomic force microscope (AFM) model XE-100 from Park Systems mounted with a probe composed of a stainless steel cantilever and a diamond tip (model DNISP from Bruker) was used to measure the nano-wear behaviour of the samples, by producing 10 scratches at 20  $\mu\text{m}$  length under 10  $\mu\text{N}$  normal force and 2  $\mu\text{m/s}$  scratching speed. Additionally, the lateral voltage output ( $M$ ), which was recorded by the position-sensitive detector of AFM, was used to calculate the friction coefficient ( $\mu$ ) as [20]

$$\mu = \alpha * M / L \quad (5)$$

where  $\alpha$  represents the conversion (calibration) factor. More details about the determination process of  $\alpha$  may be found in the respective literature [21, 22]. The Archimedes' density of the samples, which shows variety due to the Gr concentration, was determined using the density determination kit.

## 3 Results

### 3.1 Phase identification

Figure 3 shows X-ray diffraction (XRD) patterns of as-received powder (0 h) and 4 h milled powder, in



addition to as-received alloy sample (0% Gr) and Gr-reinforced composites (under 200 W laser power, 195 mm/s scanning speed, and 80  $\mu\text{m}$  hatch spacing). The machine identified only the AA2024. Neither carbon element nor iron (as a contamination element from the milling equipment) was detected, which shows that 2 wt.% stearic acid is sufficient to protect the powder from contamination from the milling equipment. Another factor can be the lower volume percentage of iron and carbon in the composite, which was lower than their detectable levels in the XRD machine. The patterns in the figure show that milling time of the powder preparation process and the addition of Gr in as-fabricated samples influence intensity. Furthermore, the main difference between powders and as-fabricated composites can be seen at  $2\theta$  values. The highest peak (at  $38^\circ$ ) for the powders was shifted to  $45^\circ$  for as-fabricated samples due to the lattice defects.

Figure 3 also shows the calculated average crystallite size (D) of the powders and as-fabricated composites. While continuous impact energy results in the reduction of crystallite size in the milled powders, the addition of Gr also leads to finer crystallite size. Previous research also demonstrates that longer milling times result in finer crystallite size [16]. Higher percentages of Gr in the as-fabricated composites also lead to gradual reduction because the addition of Gr improves the thermal conductivity and increases the dislocation density, which results in fine grain microstructure [23, 24].

### 3.2 Porosities and densities

OM images of as-fabricated composites with relation to Gr concentration from 0 to 0.5% and laser speed from 195 to 727 mm/s are shown in Fig. 4. At various scanning speeds, the pores of MMCs increase dramatically from 0.3 to 22.3% when 0.1% Gr is added. At slower scanning speeds, adding more Gr causes a reverse impact on porosity, decreasing from 22.3 to 4.1%. However, the porosity increased even further to 28.6% at faster scanning speeds. The best (see Fig. 4 c1) and the worst results (see Fig. 4 c4) among the Gr-reinforced MMCs are achieved in 0.5 wt.% Gr-reinforced composites, at different scanning speeds.

Pore size and crack length of Gr-reinforced MMCs are depicted in Fig. 5. Similar patterns have been seen in relation to scanning speed. The 0.2% Gr-reinforced composites show better results at all scanning speed parameters examined. The significant decrease in crack size for the 0.2% Gr reinforcement at slow scanning speeds illustrates the beneficial effect of Gr on crack length. The crack length pattern is nearly stable for the fast-scanning speeds. It is important to note that even though the pore sizes of the 195 mm/s scanning speed samples are essentially identical to one another, the crack length plays a key factor in the determination of the optimum parameter for the as-fabricated specimens.

Figure 6 and Fig. 7 show the relative and Archimedes' densities of as-fabricated composites, respectively. A comparison of the as-received alloy without Gr (0% Gr) and Gr-reinforced composites illustrates that the addition of Gr

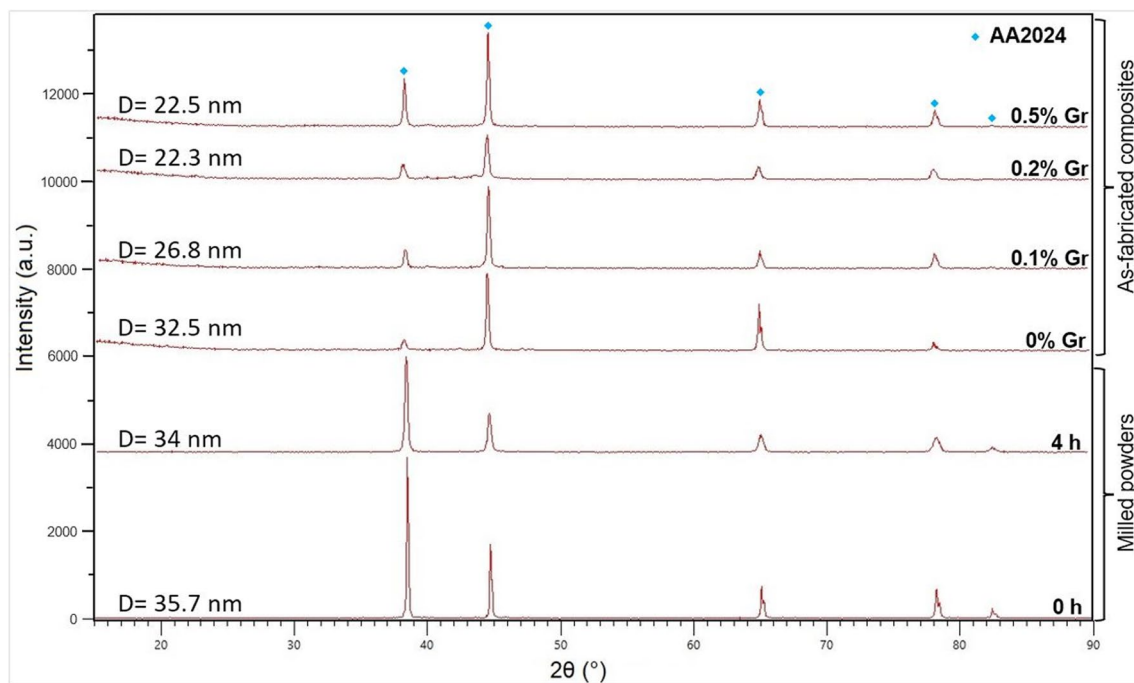
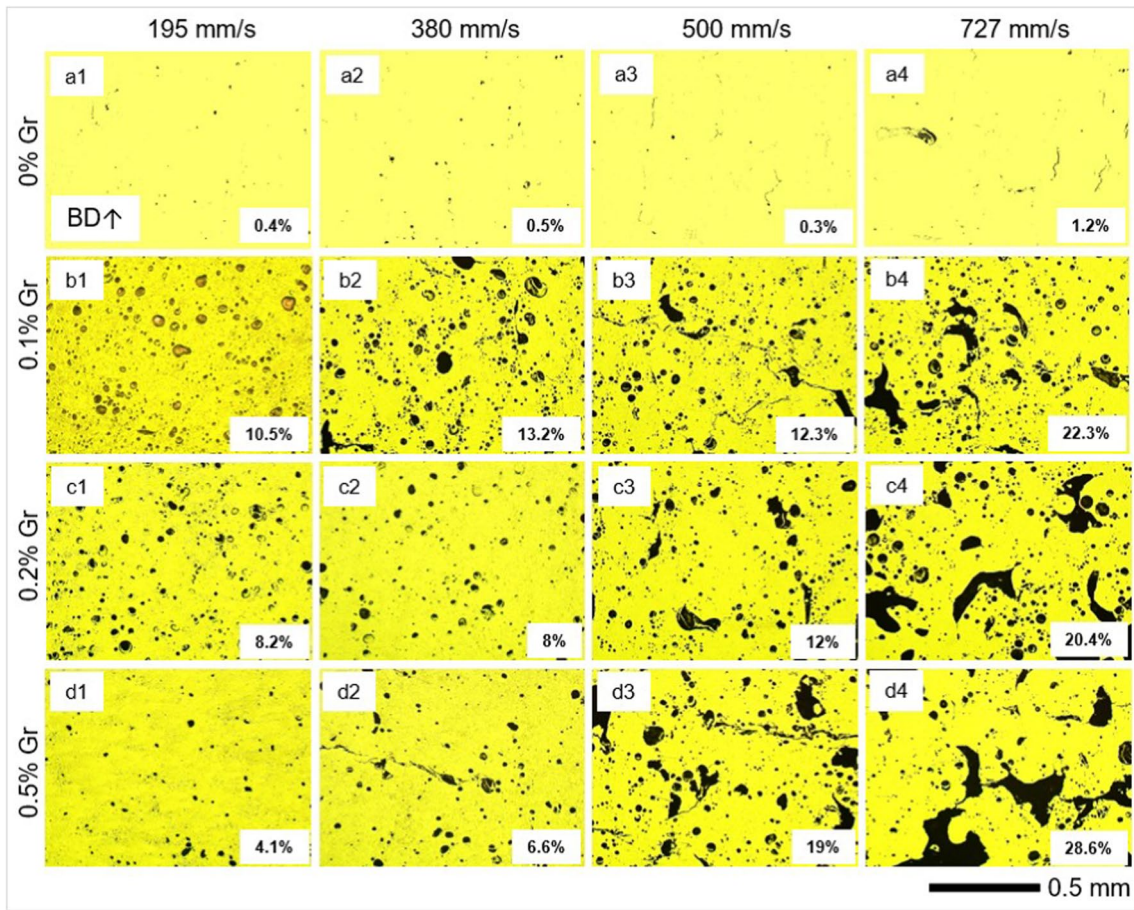
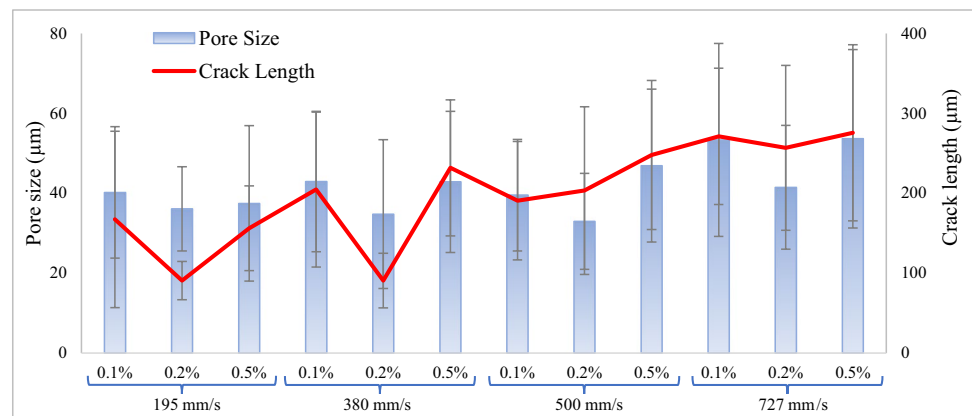


Fig. 3 XRD graph and crystallite size (D) of 0 h, 4 h milled powders, and Gr-reinforced composites



**Fig. 4** OM images showing the porosity of GNP-reinforced composites plotted against laser speed (195 to 727 mm/s) and GNP concentration (0 to 0.5 wt.%)

**Fig. 5** Pore size and crack length of 0.1 to 0.5% Gr-reinforced composites in relation to scanning speed from 195 to 727 mm/s



dramatically reduces the density of the as-fabricated composites. Additionally, the destructive effect of Gr on relative density is more obvious at faster scanning speeds (Fig. 6). In addition, Archimedes' density results show that the 0.2 wt.% Gr-reinforced composite has the best results among the other percentages across all applied scanning speeds (Fig. 7). On the other hand, Gr addition caused a severe reduction in

Archimedes' densities (between 8.8 and 17.4%) in comparison to as-received alloy due to the lesser density of the Gr.

### 3.3 Microstructure

The microstructures of the as-fabricated composites are shown in Fig. 8 and Fig. 9. Non-uniform formation of

**Fig. 6** Relative density of the composites in relation to Gr percentage and scanning speed

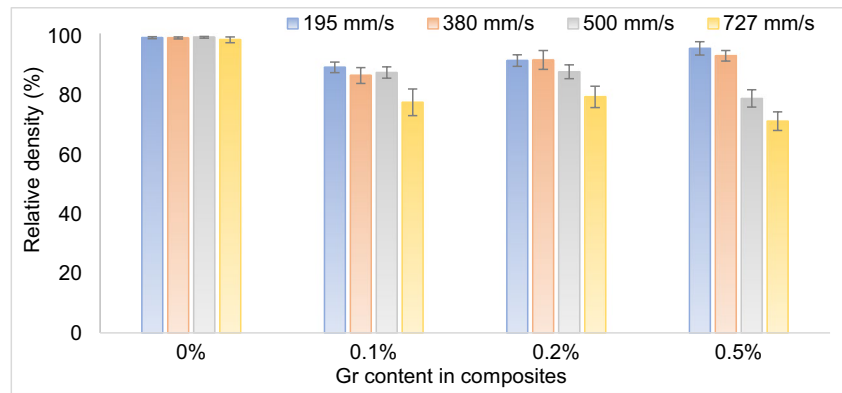
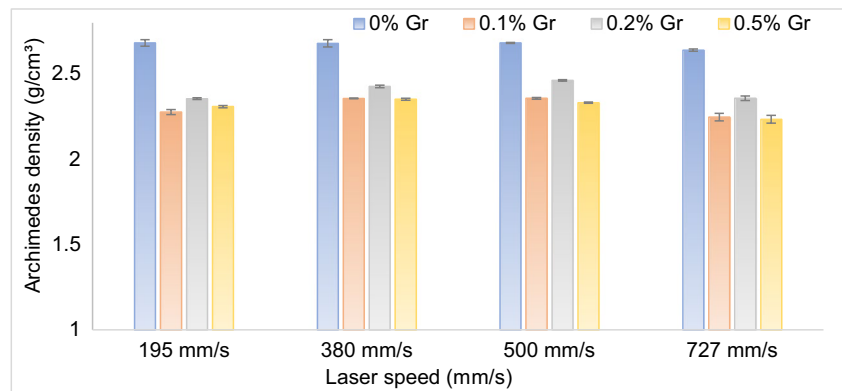


**Fig. 7** Archimedes' density of the composites in relation to laser scanning speed and Gr percentage



microstructure was obtained due to the re-melting process. Both coarse-grain and fine-grain microstructures were formed at the melt-pool. Some melt-pools were surrounded by heat-affected zone (HAZ) due to the re-melting and high laser energy. Additionally, microcracks were formed from the bottom to the top of the melt-pool because of the dendrite orientation during the cooling time. Both defects and pores are visible in OM (Fig. 8) and SEM (Fig. 9) images. Furthermore, a high cooling rate (as a result of high laser energy density) caused the trapping of non-uniform gas bubbles in the melt-pool and created spherical pores, which is unavoidable in laser-based additive manufacturing technologies [25]. On the other hand, GNPs were dissolved in MMC during the fabrication process under high laser energy. Melted carbon elements form a brittle  $Al_4C_3$  phase [10], which explains why Gr nanoparticles were not detected in the SEM images (Fig. 9).

### 3.4 Microhardness

Among the various percentages of Gr, the highest microhardness results are achieved in the 0.2 wt.% Gr-reinforced composite at all scanning speeds (see Fig. 10). In comparison to the as-received alloy (0% Gr), the addition of Gr improved the hardness up to 44.3%. This result suggests

the uniform distribution of Gr and its effective participation in composites. After the peak point (0.2 wt.%), further addition of Gr (0.5 wt.%) caused a 14% reduction at every scanning speed. This finding was also supported by the XRD results (Fig. 3), showing that the smaller crystallite size improves hardness as a result of restricted dislocation movement. This finding is also supported by the literature [25], where a 30% improvement in microhardness has also been observed in the 0.2% Gr-reinforced  $AlSi10Mg$  alloy.

Traces of the microhardness indentation tool on the observed surfaces and depth properties in the alloy and composites are shown in Fig. 11. Even though the diagonal angle of the indentation tool was  $136^\circ$ , the penetration angle on the observed surface was less than that due to the bounce back caused by elastic deformation after the indentation tool was removed [26]. More details on the finite element analysis of elastic/plastic deformation during and after indentation may be found elsewhere [27]. According to the Orowan looping mechanism, reinforced Gr in the composites reacts as an interstitial atom, which restricts the dislocation movement and improves the hardness [28]. Consequently, a higher percentage of Gr in composite results in a wider penetration angle because of the reduced ductility of the composite. Similarly, a narrower penetration angle in comparison to the indentation tool



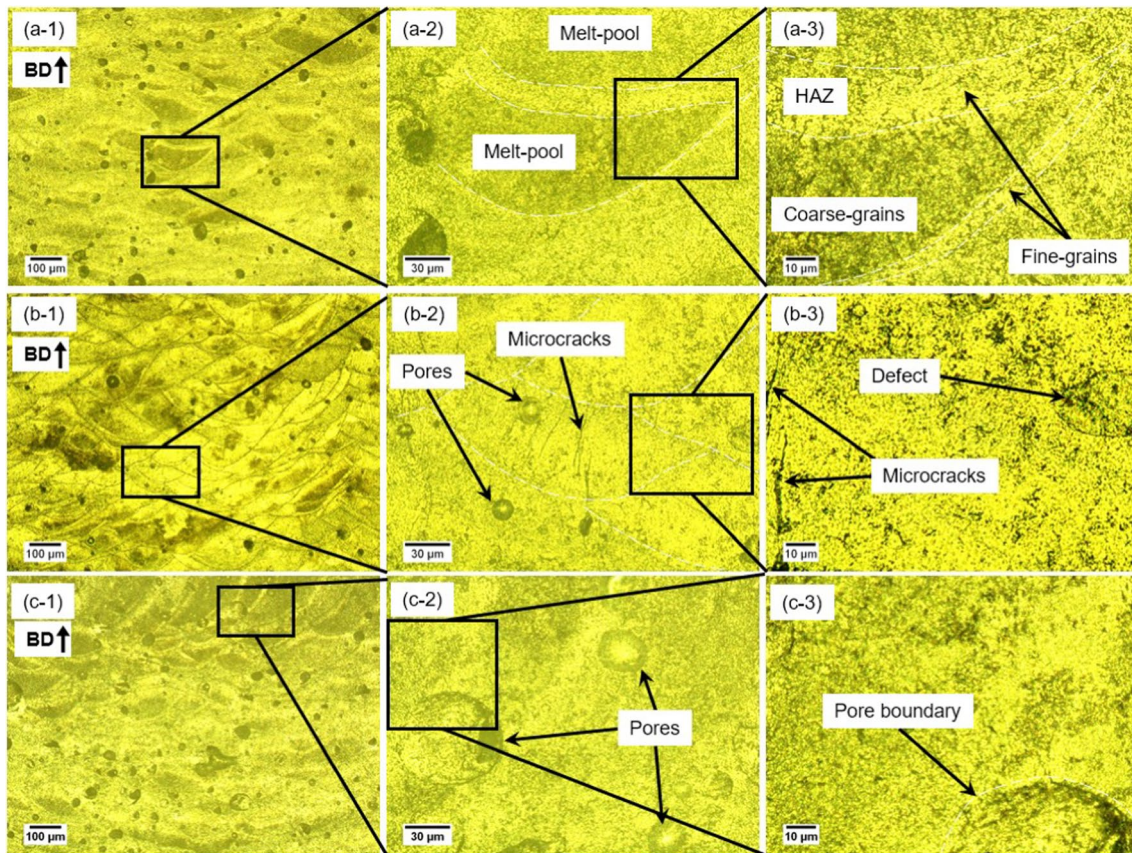


**Fig. 8** OM images showing microstructure, pores, and microcracks of **a** 0.1% Gr, **b** 0.2% Gr, and **c** 0.5% Gr-reinforced composites

dimensions has been reported in another literature study [26].

### 3.5 Pin-on-disc wear behaviour

Friction coefficients of as-received alloy (0% Gr) and Gr-reinforced composites (obtained by tribology test under 1 kg load for half an hour of sliding) are shown in Fig. 12. Despite the presence of large fluctuations at the beginning due to the vibration, nearly stable coefficient signals were observed afterwards. Relatively, similar friction coefficient patterns for the composites have been observed. In comparison to the average friction coefficient of the as-received alloy, Gr-reinforced composites offered a 60% improvement, which could be explained by the uniform distribution of Gr in the composite. Similar improvement on the tribological properties of Gr-reinforced Al6061 alloy has been reported previously [23]. Furthermore, the trend lines of the mid-points tend to plot upstream lines for the alloy and composites (except 0.5 wt.%) due to the local hardening at the friction regions. Another reason is that the highest contact has been achieved after the 13th min as a result of the deep grooves between the specimen and the wearing ball [29].

Additionally, Fig. 12 shows wear rates of the composites, which were calculated using Eq. 4. In comparison, the Gr-reinforced composites demonstrate better performance, with a proven positive effect of the Gr on the wear behaviour. While one of the reasons for this could be the uniform distribution of the reinforcement material in the composite, the other reason is that improved microhardness allows for a significant reduction in the wear rate [30]. Additionally, the 0.2 wt.% Gr-reinforced composite has the best performance among the others. However, the wear performance is reducing at the further point (0.5 wt.%). This could be explained by the 0.2 wt.% of Gr in AA2024 depicting the peak point; beyond that, the structure starts to fail due to the surpassing of the carbon amount in the composite.

### 3.6 Nano-scratch behaviour

The lateral output voltage signal of the PSPD detector built into the AFM instrument was used to detect the friction force of the AFM tip during the scratching time. Therefore, the friction coefficient was calculated from the lateral signal using Eq. 5. It can be observed from Fig. 13 that, while the lateral voltage output of the 0% and the 0.1% Gr-reinforced



**Fig. 9** SEM images showing dendrite orientation, pores, and microvoids of **a** 0.1% Gr, **b** 0.2% Gr, and **c** 0.5% Gr-reinforced composites

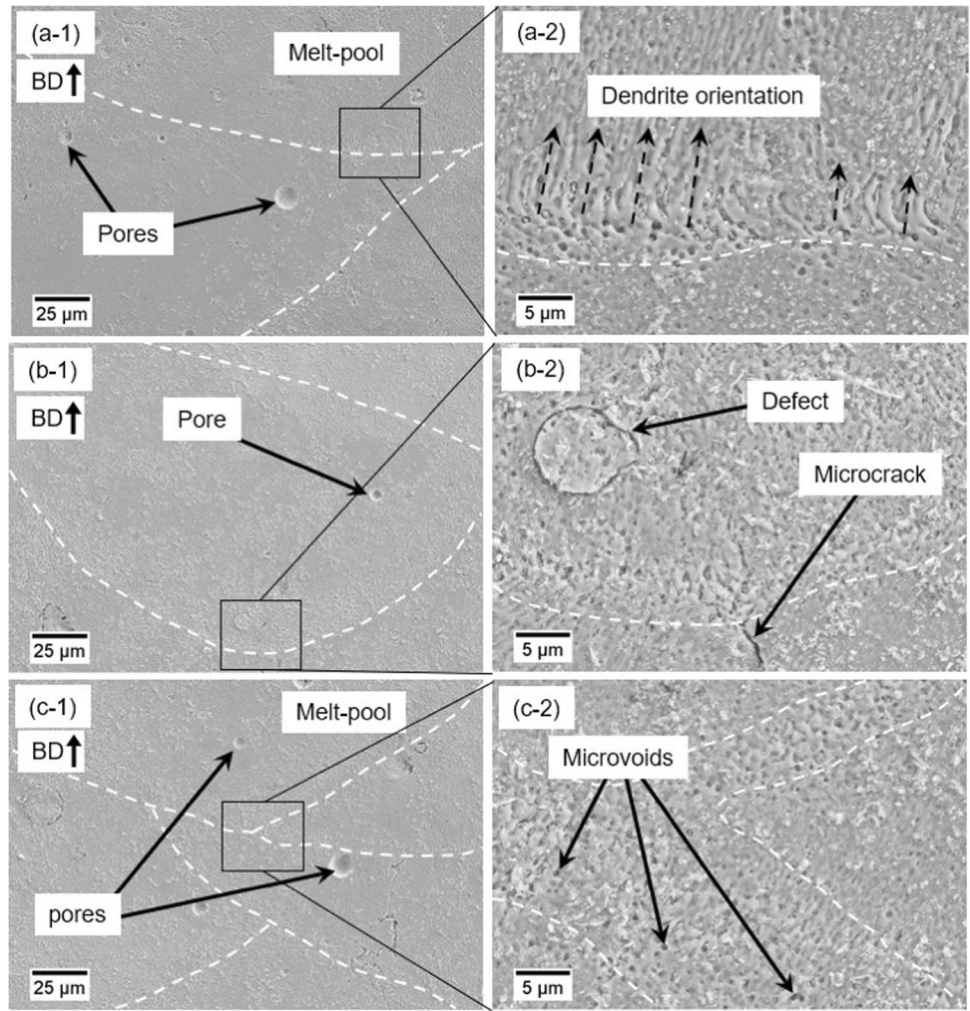
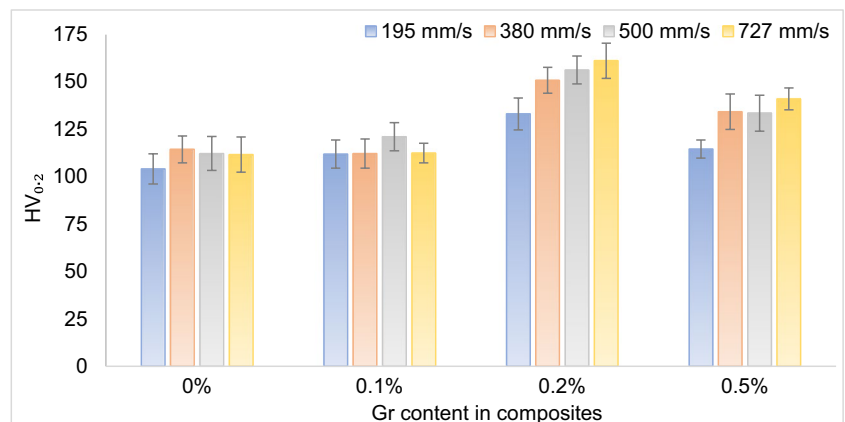


**Fig. 10** Microhardness results in as-received alloy and Gr-reinforced composites



composites display similar patterns, the other composites have substantially higher voltage owing to the hardness of the composites. The reason why the 0% and 0.1% Gr-reinforced composites have similar values is that the Gr distribution of the 0.1 wt.% Gr may not be homogeneous enough to make a difference at nanoscale. It is important to note that

composites that exhibit higher microhardness have higher friction coefficients, similar to the pin-on-disc results. While the 0% and 0.1% Gr-reinforced composites have lower friction coefficients in comparison to the pin-on-disc results, the other composites exhibit similarities. In addition, the highest output was obtained from the 0.2% Gr-reinforced composite.

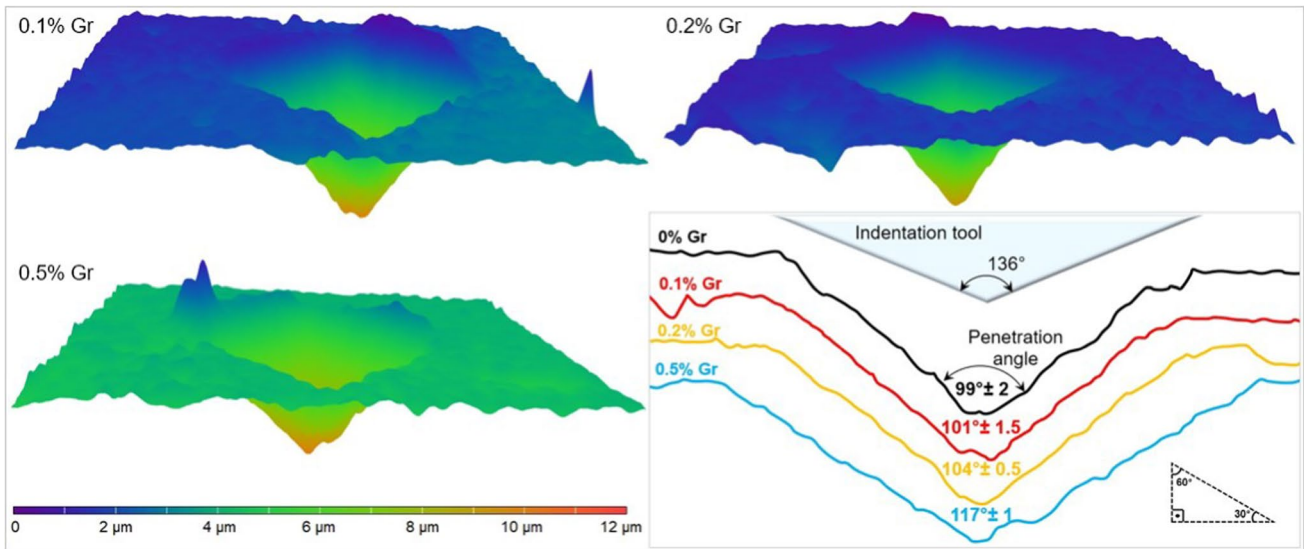


Fig. 11 OM images showing the microhardness indentation tool trace and penetration angles of Gr-reinforced composites on the surface

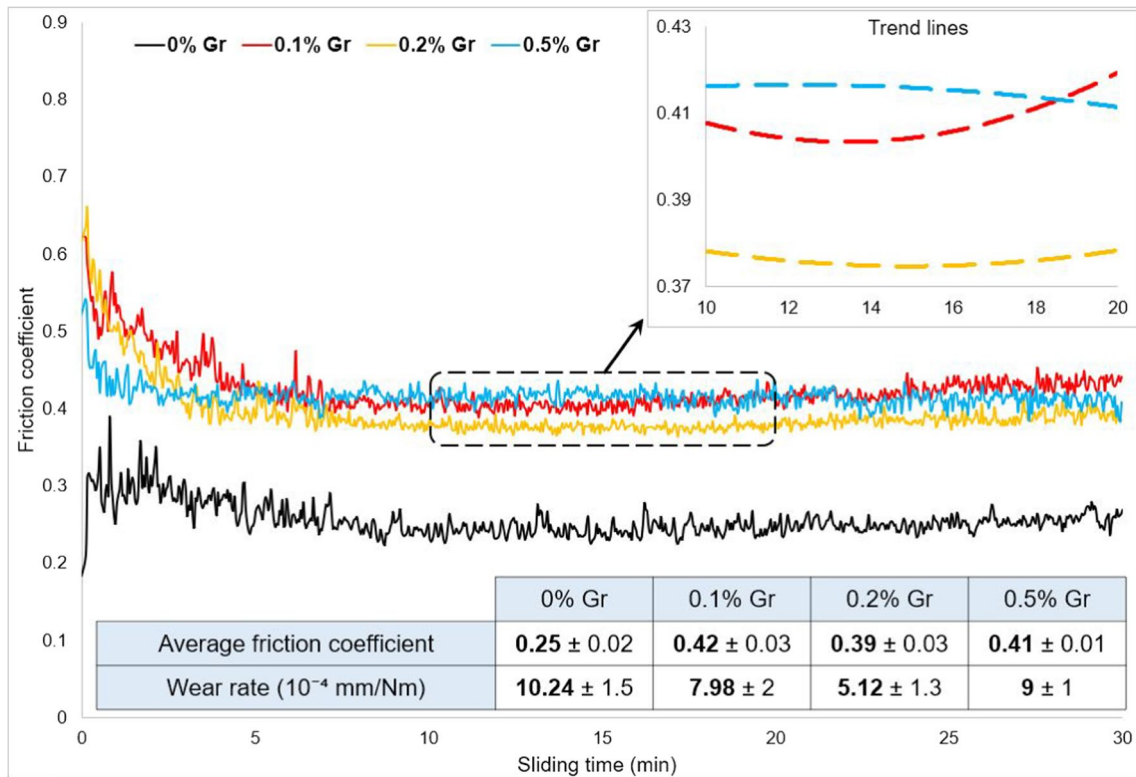


Fig. 12 Friction coefficient variation, the trend line of mid-point, and the average friction coefficient of the composites

The top view of the AFM tip and the scratches can be seen in Fig. 14. All lines are parallel to each other, and each line is 20  $\mu\text{m}$  length. The experiment has been conducted in a  $20 \times 35 \mu\text{m}^2$  area. Removed debris particles during the stretching time by the AFM tip can also be seen

at the end of the lines in Fig. 14b. As shown in Fig. 13, at the beginning of the scratch (0 to 0.5 s), the AFM tip is subjected to large fluctuations until the instruments adjust the required force (10  $\mu\text{N}$ ). After this point, the line is smoother until the end (10th s).

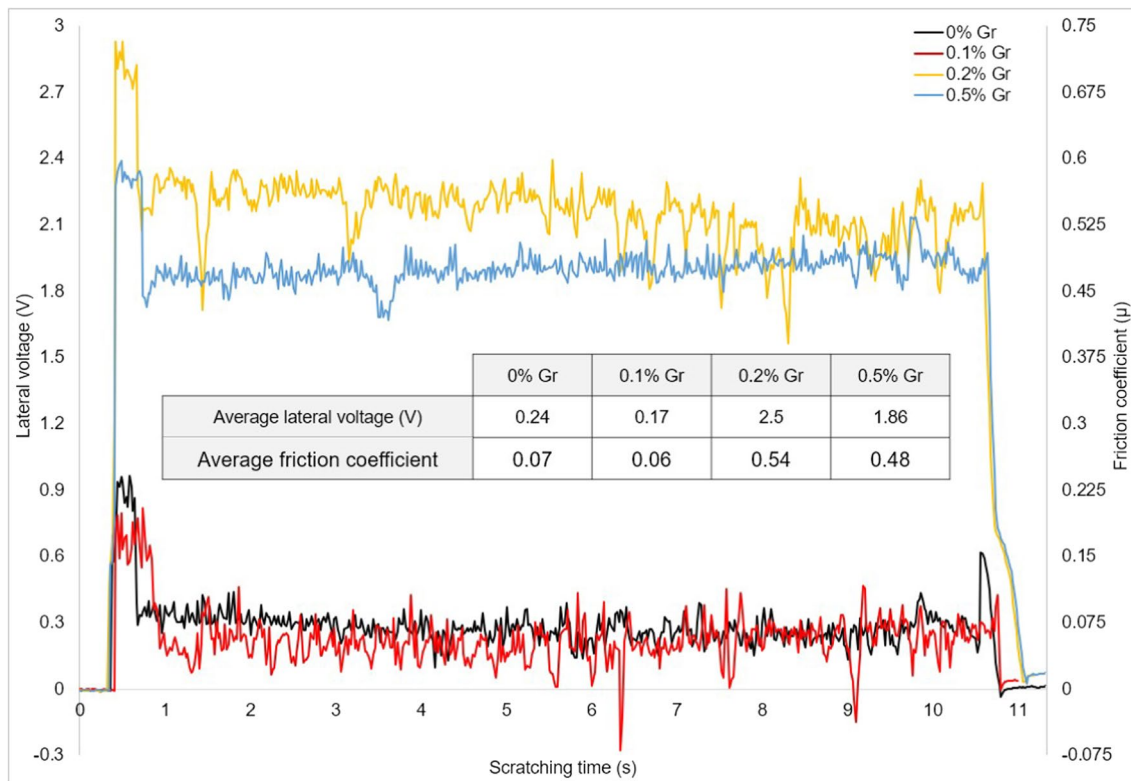
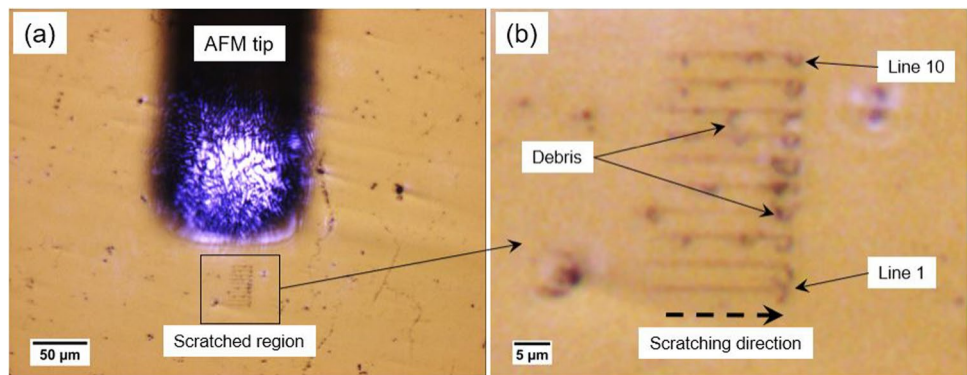


Fig. 13 Lateral voltage outputs and average lateral signals of the composites

Fig. 14 AFM images showing the top view of the tip and the scratches



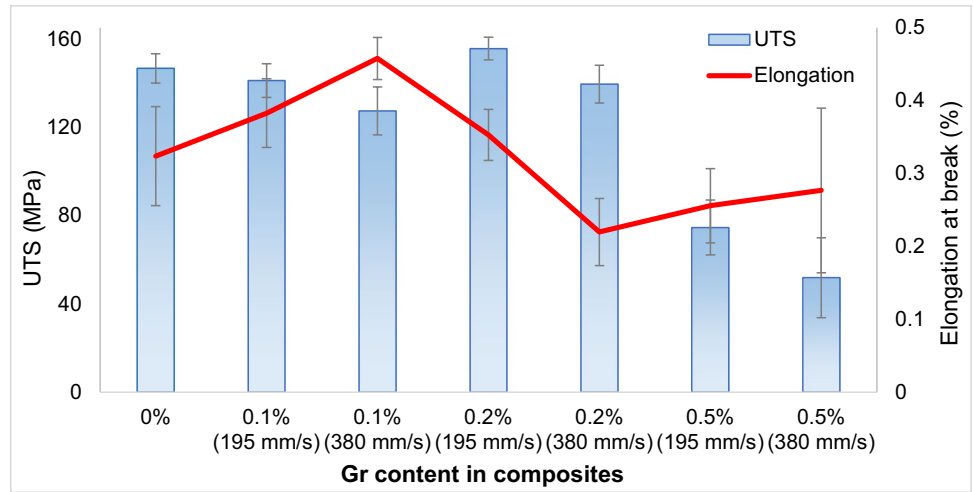
### 3.7 Mechanical properties

The tensile properties of the as-received alloy (0% Gr) [18] and Gr-reinforced composites are shown in Fig. 15. Both 195 and 380 mm/s scanning speeds have been examined due to the better relative and Archimedes’ densities of the cubic specimens. While the 0.2% Gr-added composite depicts slight improvement (6.2%) at 195 mm/s, 0.1% and 0.5% Gr-reinforced composites resulted in a reduction (4% and 50%, respectively) of UTS in comparison to the 0% Gr. It is important to note that despite the severe reduction in density (8%) of the composite from the 0 to 0.2% Gr-reinforced composites, the tensile strength showed

improvement. However, faster scanning speeds resulted in lower UTS at all Gr concentrations due to insufficient energy density. Additionally, percentages of Gr above and below 0.2 wt.% result in reductions. This may be due to the fact that the adequate percentage of Gr in the composite leads to improved mechanical properties of the composite. In addition, the uniform distribution of the Gr in the composite could be another reason that positively affects the tensile property. On the other hand, despite the lesser reduction (4%) of density between the 0 and the 0.5% Gr-reinforced composites, tensile strength showed dramatic reduction (50%) due to the exceeded concentration of the carbon element. On the other hand, the composites’ low elongation at



**Fig. 15** Ultimate tensile strength and elongation of the as-received alloy (0%) [18] and the Gr-reinforced composites using 195 and 380 mm/s scanning speeds



break validates the tensile test specimens' brittleness. The brittleness of the composite is highly influenced by its high relative crack susceptibility and porosity, which is enhanced with the addition of Gr.

SEM images of the fracture surface of the composites fabricated under 195 mm/s scanning speed and 200 W laser power are shown in Fig. 16. Similar fracture microstructure on the observed surfaces can be seen for the composites.

Pores and inner cracks that cause an early failure of the sample in the tensile tests are highlighted with arrows. Even though high laser energy was used during the fabrication process, several unmelted powders and powder holes (pores) on the observed surface can still be seen in Fig. 16 (which suggests that a higher laser power than 200 W might be required for the composites to reduce unmelted powder in the structure). Additionally, dimple structure and cleavage

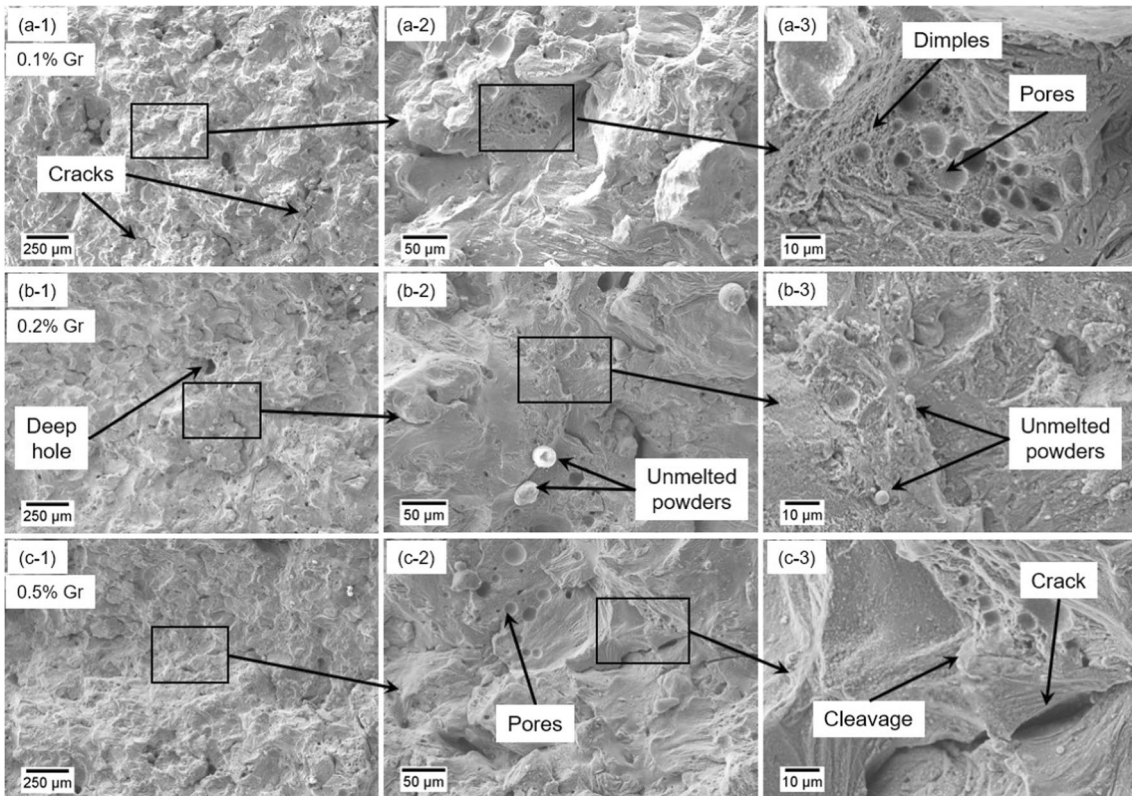


**Fig. 16** SEM images of the fracture surface showing pores, cracks, and unmelted powders

can be seen locally. Zoomed SEM images of the 0.2% Gr-reinforced composite are shown in Fig. 17 in order to see the dimple structure. Very fine dimple structures (dimple size: 0.1 to 2  $\mu\text{m}$ ), which also implied ductile behaviour, have been observed from the fracture surface [11, 31].

#### 4 Discussion

Previous research shows that the milling time and Gr addition have a direct effect on the crystallite refinement [32]. In particular, the effect of the milling time on the phase identification was investigated, and it had been reported that continuous impact energy in the milling bowl causes more lattice defects in powder as a consequence of severe cold-working and plastic deformation. This study shows that a higher amount of Gr improves the crystallite density (see Fig. 3). This is due to the contribution of Gr subsequent to the fabrication in the pinning of the displacements, which produces further strain in the matrix [25]. The peak shift and broadenings following the fabrication can also be explained by the incredibly high cooling rate and the existence of a Gr-related increase in the dislocation density as a result of induced lattice strain [33].

Therewith, the finer grain and crystallite size results in a higher number of grain and crystallite boundaries, which improve the mechanical properties by restricting the movement of dislocations [2] and causing dislocation shift of pileup at  $2\theta$  values from 38 to 45° (see Fig. 3). Additionally, better heat distribution of the Gr-reinforced composites has been reported due to the elevated thermal conductivity of Gr (5000 W/mK) [34], which is substantially higher than of AA2024 (194 W/mK) [35]. The presence of Gr in the

composite enhances the thermal conductivity and cooling rate of the composite due to the excellent thermal conductivity of the Gr which results in finer grain structures [36]. It has been reported that the wear performance of materials is directly related to grain refinement, microstructure, and microhardness [37]. Hence, the higher cooling rates trigger greater dislocation density, resulting in the finer crystallite size, seen in the as-fabricated composites in Fig. 3.

The porosity was significantly increased with the 0.1% Gr reinforcement (see Fig. 4). One reason for increase is that Gr-reinforced MMCs require higher energy density (energy per unit volume) than bare alloy [25]. Insufficient and low energy density at faster scanning speeds led to higher porosity in Gr-reinforced specimens, as expected. Surprisingly, further addition of Gr at slower scanning speeds (195 and 380 mm/s), however, resulted in a better outcome than at faster scanning speeds (500 and 727 mm/s). The reason behind this slight improvement at slow scanning speed can be explained by the high thermal conductivity and large surface area of Gr that allow the MMCs to absorb more laser energy to meet the required energy for the Gr-reinforced MMCs [36]. Furthermore, Gr agglomeration prior to LPBF results in a significant variation in the melting points of Al and Gr as well as a significant density difference between the components [38]. Moreover, increased Gr content in composite further reduces the density of the composite (see Fig. 4).

Pore size and crack length measurements revealed that slower scanning speeds (195 and 380 mm/s) lead to smaller cracks on the observation surface (see Fig. 5). At each scanning speed, the smallest crack length values are obtained from 0.2% Gr-reinforced composites. Exceeding the Gr percentage in MMCs results in larger cracks and pore sizes.

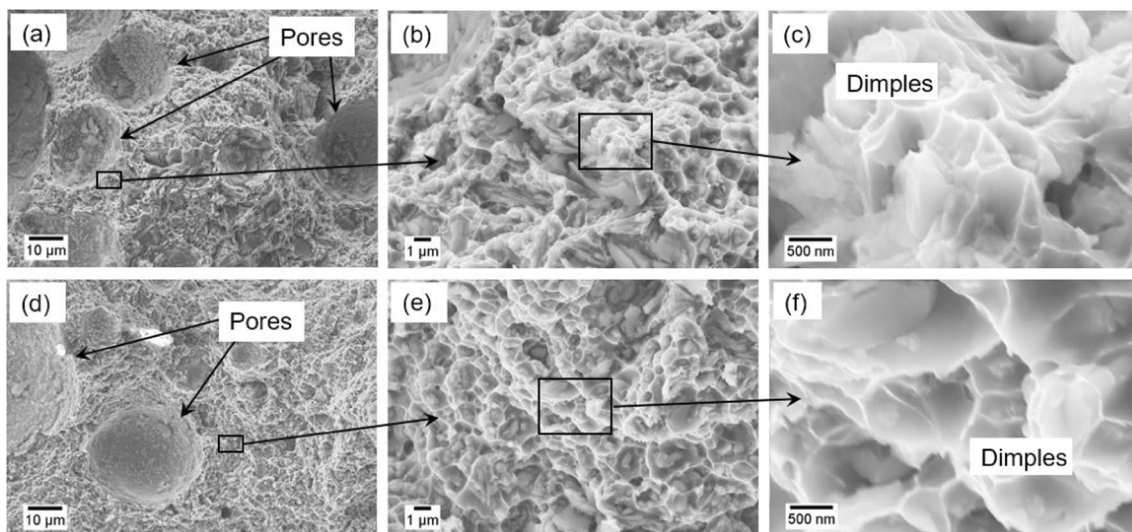


Fig. 17 Fracture surface of the 0.2% Gr-reinforced composite showing pores and dimples on the nanoscale

The relative and Archimedes' densities show a similar pattern until the 0.2 wt.%, which can be explained by the uniformity of the layers (Fig. 6 and Fig. 7). While Archimedes' density quantifies the density of a cube for each parameter, the relative density is obtained from the three separate layers of each specimen utilising OM images and ImageJ software. Similarly, the big difference between Archimedes' density and the relative density at 0.5 wt.% can also be explained as the non-uniformity of the layers. On the other hand, in comparison with Archimedes' density of the as-received alloy and the as-fabricated composites, Gr reinforcement results in a severe reduction (Fig. 7) for two reasons. First, more pores are formed in composites with the addition of Gr, and thus, Archimedes' density results are reduced, which is consistent with others [25, 30, 39]. Another explanation for this decrease is that GNPs absorb gaseous components (such as oxygen and nitrogen) and generate porosity in the structure and therefore lowering Archimedes' density [40]. Furthermore, the addition of lighter reinforcement material and mixing parameters can reduce the density of the composites owing to the density and cold-welding [32]. The combination of these effects generates a difference between the as-received alloy and Gr-reinforced composites. Furthermore, different measurement and estimation techniques (such as relative and Archimedes' densities) may also result in different patterns.

OM (see Fig. 8) and SEM images (see Fig. 9) are used to investigate the microstructure of as-fabricated specimens. Due to variable temperature gradients and solidification rates throughout the cooling process in the melt pool, both fine- and coarse-grained microstructures are apparent [41]. At higher Gr concentrations, coarser-grained microstructure is more prominent (see Fig. 8). It has been reported that higher energy density in the melt pool results in an increase in the solidification rate as well as coarse-grained microstructure [41]. Further increasing the Gr concentration in the MMCs increases the thermal conductivity of the composite, which leads it to absorb more energy from the applied laser beam in the melt pool.

The addition of Gr improved the microhardness of the as-fabricated composites by 45% (at 0.2% Gr) (see Fig. 10). This enhancement demonstrates Gr's effective contribution to grain refinement (see Fig. 3) [25]. However, the high porosity intensity at 0.5% Gr reduced the microhardness of the as-fabricated sample [42]. Similarly, the negative effect of the high percentage of Gr on microhardness has been previously reported [43]. Additionally, while the 0% and 0.1% Gr-reinforced specimens were almost unaffected by scanning speed, the positive effect of the scanning speed on the microhardness can be seen after 0.2% Gr. The reason for this improvement in fast scanning speed can be attributed to the solidification rate. Slow scanning speeds cause an increase in solidification time, which results in a coarser

microstructure [44]. Contrary to this, fast scanning speeds reduce the solidification time and form a finer microstructure that restricts the dislocation movement [45]. The elasticity of the fabricated specimens is also impacted by the composite's microstructure (see Fig. 11). The ductility of the specimens decreases parallel to the rise in microhardness at higher Gr concentrations.

Tribology (pin-on-disc) testing demonstrates that the addition of Gr improves the wear performance of the composites (see Fig. 12). The friction output voltage was increased depending upon hardness. Parallel to microhardness results, 0.2% Gr-reinforced composite provides 56% higher output voltage. Additionally, trend lines of the mid-points demonstrate that the output voltage gradually improves after a certain point. The reason for this change on the trend lines is that the milling ball creates deeper grooves in the process, which increases the surface contact and generates additional temperature at the friction region [29]. Higher temperature results in the local hardening, and thus, friction coefficient starts to increase slightly [29]. Similarly, the wear rates of the composites have better performance in comparison to the as-received alloy due to the better hardness.

A comparison of the AFM and the pin-on-disc tests demonstrates that while AFM friction coefficients of 0.2% and 0.5% Gr-reinforced composites show similarities, values of the other composites are lower in the AFM results. AFM tests have been conducted in a  $20 \times 35 \mu\text{m}^2$  area. At this scale, nano cracks, keyhole pores, and balling effects (see Fig. 8 and Fig. 9) may strongly influence the outcome of the AFM test (see Fig. 13) [19]. This might be the explanation for why the 0% and 0.1% Gr-reinforced composites are lower than the pin-on-disc results.

On the other hand, for all Gr contents, a scanning speed of 195 mm/s leads to superior tensile properties than 380 mm/s (see Fig. 15). It is a well-known fact that increased porosity as a result of faster scanning speed leads to a considerable loss of strength [46]. A severe reduction in the tensile testing recordings of 0.1% and 0.5% Gr-reinforced composites illustrate the significant effect of the porosity and cracks in comparison to the as-received alloy. However, the 0.2% Gr-reinforced composite shows that a certain amount of Gr can improve the mechanical properties of the composite.

## 5 Conclusion

The present study investigated the effect of scanning speed and Gr concentration on microstructure and mechanical characteristics of the GNPs/AA2024 composites fabricated using LPBF. The effect of crack and pore formation on the mechanical properties was also identified, and the following key findings were drawn from the experimental data:



- a) Not only milling the powder but also adding the Gr decreased the crystallite size due to the enhanced thermal conductivity of the composite with the addition of Gr. The addition of 0.2% Gr resulted in a 37.6% reduction in crystallite size compared to the as-received alloy.
- b) Microhardness of the as-fabricated composites was improved up to 45% parallel to the Gr concentration. This indicates that Gr is distributed evenly throughout the structure. Additionally, the faster scanning speed is another positive effect on the improvement of the microhardness due to the high solidification rate resulting in a finer microstructure.
- c) Due to the greater laser power requirements of the new composites, the addition of Gr causes an increase in the porosity of the composites. The best density (95.6%) has been achieved from 195 mm/s scanning speed and the 0.5% Gr-reinforced composite. Even though the porosity of the sample has risen, the ultimate tensile strength of 0.2% Gr was marginally enhanced (7%).
- d) Both macro (pin-on-disc) and nano (AFM) wear performance of the composites improved gradually with the addition of Gr. The 0.2% Gr had a 50% and 56% superior wear rate and average friction coefficient ( $\mu$ ) performance than the 0% Gr due to uniform distribution and improved hardness of the composite.

These results indicate a significant finding that adding Gr to a composite fabricated using LPBF increases porosity and causes more cracks; however, a certain amount of Gr reinforcement can result in better mechanical properties (microstructure, wear performance, and tensile strength). Another important finding of this study is that the wear behaviour of the same composite might exhibit different performance at the macro and nanoscale. In terms of mechanical performance, 0.2% Gr-reinforced AA2024 composite has been recommended for LPBF under the applied fabrication parameters. Future work includes investigating the suitability of the new composite for advanced engineering applications.

**Author contributions** Mulla Ahmet Pekok: writing original draft, review and editing, visualization, methodology, investigation, software, formal analysis, and conceptualization. Rositza Setchi: review and editing, methodology, supervision, formal analysis, project administration, and data curation. Michael Ryan: review and editing, methodology, supervision, and data curation. Emmanuel Brousseau: review and editing, and data curation. Dongdong Gu: review and editing, and methodology.

**Funding** This research was sponsored by the Ministry of National Education of Turkey and ASTUTE 2020 (Advanced Sustainable Manufacturing Technologies). This operation, supporting manufacturing companies across Wales, has been part-funded by the European Regional Development Fund through the Welsh Government and the participating Higher Education Institutions.

## Declarations

**Competing interests** The authors declare no competing interests.

**Open Access** This article is licensed under a Creative Commons Attribution 4.0 International License, which permits use, sharing, adaptation, distribution and reproduction in any medium or format, as long as you give appropriate credit to the original author(s) and the source, provide a link to the Creative Commons licence, and indicate if changes were made. The images or other third party material in this article are included in the article's Creative Commons licence, unless indicated otherwise in a credit line to the material. If material is not included in the article's Creative Commons licence and your intended use is not permitted by statutory regulation or exceeds the permitted use, you will need to obtain permission directly from the copyright holder. To view a copy of this licence, visit <http://creativecommons.org/licenses/by/4.0/>.

## References

1. Papageorgiou DG, Kinloch IA, Young RJ (2017) Mechanical properties of graphene and graphene-based nanocomposites. *Prog Mater Sci* 90:75–127. <https://doi.org/10.1016/j.pmatsci.2017.07.004>
2. Nieto A, Bisht A, Lahiri D et al (2017) Graphene reinforced metal and ceramic matrix composites: a review. *Int Mater Rev* 62:241–302. <https://doi.org/10.1080/09506608.2016.1219481>
3. Wang P, Eckert J, Prashanth KG, Wu MW, Kaban I, Xi LX, Scudino S (2020) A review of particulate-reinforced aluminum matrix composites fabricated by selective laser melting. *Trans Nonferrous Metals Soc China* 30(8):2001–2034. [https://doi.org/10.1016/S1003-6326\(20\)65357-2](https://doi.org/10.1016/S1003-6326(20)65357-2)
4. Gu DD, Meiners W, Wissenbach K, Poprawe R (2012) Laser additive manufacturing of metallic components: materials, processes and mechanisms. *Int Mater Rev* 57:133–164. <https://doi.org/10.1179/1743280411Y.0000000014>
5. Zhang B, Li Y, Bai Q (2017) Defect formation mechanisms in selective laser melting: a review. *Chinese J Mech Eng (English Ed)* 30:515–527. <https://doi.org/10.1007/s10033-017-0121-5>
6. AbuShanab WS, Moustafa EB, Ghandourah E, Taha MA (2020) Effect of graphene nanoparticles on the physical and mechanical properties of the Al2024-graphene nanocomposites fabricated by powder metallurgy. *Results Phys* 19:103343. <https://doi.org/10.1016/j.rinp.2020.103343>
7. Shin SE, Ko YJ, Bae DH (2016) Mechanical and thermal properties of nanocarbon-reinforced aluminum matrix composites at elevated temperatures. *Compos Part B Eng* 106:66–73. <https://doi.org/10.1016/j.compositesb.2016.09.017>
8. Bilisik K, Akter M (2021) Graphene nanoplatelets/epoxy nanocomposites: a review on functionalization, characterization techniques, properties, and applications. *J Reinf Plast Compos* 073168442110492. <https://doi.org/10.1177/07316844211049277>
9. Pourmand NS, Asgharzadeh H (2020) Aluminum matrix composites reinforced with graphene: a review on production, microstructure, and properties. *Crit Rev Solid State Mater Sci* 45:289–337. <https://doi.org/10.1080/10408436.2019.1632792>
10. Huang CY, Hu SP, Chen K (2019) Influence of rolling temperature on the interfaces and mechanical performance of graphene-reinforced aluminum-matrix composites. *Int J Miner Metall Mater* 26:752–759. <https://doi.org/10.1007/s12613-019-1780-2>
11. Hu Z, Chen F, Xu J et al (2018) 3D printing graphene-aluminum nanocomposites. *J Alloys Compd* 746:269–276. <https://doi.org/10.1016/j.jallcom.2018.02.272>

12. Güler Ö, Bağcı N (2020) A short review on mechanical properties of graphene reinforced metal matrix composites. *J Mater Technol* 9:6808–6833. <https://doi.org/10.1016/j.jmrt.2020.01.077>
13. Anthony Xavier M, Prashantha Kumar HG (2017) Processing and characterization techniques of graphene reinforced metal matrix composites (GRMMC); a review. *Mater Today Proc* 4:3334–3341. <https://doi.org/10.1016/j.matpr.2017.02.220>
14. Gisario A, Kazarian M, Martina F, Mehrpouya M (2019) Metal additive manufacturing in the commercial aviation industry: a review. *J Manuf Syst* 53:124–149. <https://doi.org/10.1016/j.jmsy.2019.08.005>
15. Ngo TD, Kashani A, Imbalzano G et al (2018) Additive manufacturing (3D printing): a review of materials, methods, applications and challenges. *Compos Part B Eng* 143:172–196. <https://doi.org/10.1016/j.compositesb.2018.02.012>
16. Pekok MA, Setchi R, Ryan M et al (2022) Al-Cu-Mg alloy powder reinforced with graphene nanoplatelets: morphology, flowability and discrete element simulation. *J Manuf Mater Process* 6:148. <https://doi.org/10.3390/jmmp6060148>
17. Pekok M, Setchi R, Ryan M, Han Q (2020) Effect of milling speed and time on graphene-reinforced AA2024 powder. Springer Singapore
18. Pekok MA, Setchi R, Ryan M et al (2021) Effect of process parameters on the microstructure and mechanical properties of AA2024 fabricated using selective laser melting. *Int J Adv Manuf Technol* 112:175–192. <https://doi.org/10.1007/s00170-020-06346-y>
19. Han Q, Geng Y, Setchi R et al (2017) Macro and nanoscale wear behaviour of Al-Al<sub>2</sub>O<sub>3</sub> nanocomposites fabricated by selective laser melting. *Compos Part B Eng* 127:26–35. <https://doi.org/10.1016/j.compositesb.2017.06.026>
20. Wang H, Gee ML (2014) AFM lateral force calibration for an integrated probe using a calibration grating. *Ultramicroscopy* 136:193–200. <https://doi.org/10.1016/j.ultramicro.2013.10.012>
21. Boland MJ, Hempel JL, Ansary A et al (2018) Graphene used as a lateral force microscopy calibration material in the low-load non-linear regime. *Rev Sci Instrum* 89:113902. <https://doi.org/10.1063/1.5044727>
22. Xie H, Onal C, Régnier S, Sitti M (2012) Atomic force microscopy based nanorobotics. Springer, Berlin Heidelberg, Berlin, Heidelberg
23. Zhang H, Zhang B, Gao Q et al (2021) A review on microstructures and properties of graphene-reinforced aluminum matrix composites fabricated by friction stir processing. *J Manuf Process* 68:126–135. <https://doi.org/10.1016/j.jmapro.2021.07.023>
24. Pireyousefan MK, Rahmaniard R, Orovčík L et al (2020) Application of a novel method for fabrication of graphene reinforced aluminum matrix nanocomposites: synthesis, microstructure, and mechanical properties. *Mater Sci Eng A* 772:138820. <https://doi.org/10.1016/j.msea.2019.138820>
25. Tiwari JK, Mandal A, Sathish N et al (2020) Investigation of porosity, microstructure and mechanical properties of additively manufactured graphene reinforced AlSi10Mg composite. *Addit Manuf* 33:1–12. <https://doi.org/10.1016/j.addma.2020.101095>
26. Mukhopadhyay NK, Weatherly GC, Embury JD (2001) An analysis of microhardness of single-quasicrystals in the Al-CU-Co-Si system. *Mater Sci Eng A* 315:202–210. [https://doi.org/10.1016/S0921-5093\(01\)01186-8](https://doi.org/10.1016/S0921-5093(01)01186-8)
27. Giannakopoulos AE, Suresh S (1999) Determination of elastoplastic properties by instrumented sharp indentation. *Scr Mater* 40:1191–1198. [https://doi.org/10.1016/S1359-6462\(99\)00011-1](https://doi.org/10.1016/S1359-6462(99)00011-1)
28. Raj RR, Yoganandh J, Saravanan MSS, Kumar SS (2021) Effect of graphene addition on the mechanical characteristics of AA7075 aluminium nanocomposites. *Carbon Lett* 31:125–136. <https://doi.org/10.1007/s42823-020-00157-7>
29. Yu T, Liu J, He Y et al (2021) Microstructure and wear characterization of carbon nanotubes (CNTs) reinforced aluminum matrix nanocomposites manufactured using selective laser melting. *Wear* 476. <https://doi.org/10.1016/j.wear.2020.203581>
30. Manjunath N, Manjunath LH, Vinayak M et al (2021) Effect of microstructure, mechanical and wear on Al-CNTs/graphene hybrid MMC'S. *Adv Mater Process Technol* 00:1–14. <https://doi.org/10.1080/2374068X.2021.1927646>
31. Han Q, Mertens R, Montero-Sistiaga ML et al (2018) Laser powder bed fusion of Hastelloy X: effects of hot isostatic pressing and the hot cracking mechanism. *Mater Sci Eng A* 732:228–239. <https://doi.org/10.1016/j.msea.2018.07.008>
32. Akçamlı N, Küçükelyas B, Kaykılarlı C, Uzunsoy D (2019) Investigation of microstructural, mechanical and corrosion properties of graphene nanoplatelets reinforced Al matrix composites. *Mater Res Express* 6:115627. <https://doi.org/10.1088/2053-1591/ab511f>
33. Mandal A, Tiwari JK, Sathish N, Srivastava AK (2020) Microstructural and mechanical properties evaluation of graphene reinforced stainless steel composite produced via selective laser melting. *Mater Sci Eng A* 774:138936. <https://doi.org/10.1016/j.msea.2020.138936>
34. Dorri Moghadam A, Omrani E, Menezes PL, Rohatgi PK (2015) Mechanical and tribological properties of self-lubricating metal matrix nanocomposites reinforced by carbon nanotubes (CNTs) and graphene - a review. *Compos Part B Eng* 77:402–420. <https://doi.org/10.1016/j.compositesb.2015.03.014>
35. Chen L, Qi Y, Fei Y, Du Z (2021) Enhanced mechanical properties and thermal conductivity for GNPs/Al2024 composites with in situ SiC nanorods. *Met Mater Int* 27:4263–4270. <https://doi.org/10.1007/s12540-020-00803-9>
36. Aboulkhair NT, Simonelli M, Parry L et al (2019) 3D printing of aluminium alloys: additive manufacturing of aluminium alloys using selective laser melting. *Prog Mater Sci* 106:100578. <https://doi.org/10.1016/j.pmatsci.2019.100578>
37. Prashanth KG, Debalina B, Wang Z et al (2014) Tribological and corrosion properties of Al–12Si produced by selective laser melting. *J Mater Res* 29:2044–2054. <https://doi.org/10.1557/jmr.2014.133>
38. Lava Kumar P, Lombardi A, Byczynski G et al (2022) Recent advances in aluminium matrix composites reinforced with graphene-based nanomaterial: a critical review. *Prog Mater Sci* 128:100948. <https://doi.org/10.1016/j.pmatsci.2022.100948>
39. Liu X, Zhao C, Zhou X et al (2019) CNT-reinforced AlSi10Mg composite by selective laser melting: microstructural and mechanical properties. *Mater Sci Technol (United Kingdom)* 35:1038–1045. <https://doi.org/10.1080/02670836.2019.1603899>
40. Xia H, Zhang L, Zhu Y et al (2020) Mechanical properties of graphene nanoplatelets reinforced 7075 aluminum alloy composite fabricated by spark plasma sintering. *Int J Miner Metall Mater* 27:1295–1300. <https://doi.org/10.1007/s12613-020-2009-0>
41. Maamoun AH, Xue YF, Elbestawi MA, Veldhuis SC (2018) The effect of selective laser melting process parameters on the microstructure and mechanical properties of Al6061 and AlSi10Mg alloys. *Materials (Basel)* 12. <https://doi.org/10.3390/ma12010012>
42. Bai P, Jin Y, Zhao Z et al (2019) Microstructure and tribological behavior of graphene/Al composites produced by selective laser melting. *Mater Res Express* 6. <https://doi.org/10.1088/2053-1591/ab3ef5>
43. Azar MH, Sadri B, Nematı A et al (2019) Investigating the microstructure and mechanical properties of aluminum-matrix reinforced-graphene nanosheet composites fabricated by mechanical milling and equal-channel angular pressing. *Nanomaterials* 9:1–17. <https://doi.org/10.3390/nano9081070>

44. Zhang J, Song B, Wei Q et al (2019) A review of selective laser melting of aluminum alloys: processing, microstructure, property and developing trends. *J Mater Sci Technol* 35:270–284. <https://doi.org/10.1016/j.jmst.2018.09.004>
45. Larimian T, Kannan M, Grzesiak D et al (2020) Effect of energy density and scanning strategy on densification, microstructure and mechanical properties of 316L stainless steel processed via selective laser melting. *Mater Sci Eng A* 770:138455. <https://doi.org/10.1016/j.msea.2019.138455>
46. Wang Y, Shi J, Lu S, Xiao W (2018) Investigation of porosity and mechanical properties of graphene nanoplatelets-reinforced AlSi10Mg by selective laser melting. *J Micro Nano-Manufacturing* 6:1–7. <https://doi.org/10.1115/1.4038454>

**Publisher's note** Springer Nature remains neutral with regard to jurisdictional claims in published maps and institutional affiliations.